

Research Article

High-Resolution ISAR Imaging with Wideband V-FM Waveforms

Dejun Feng,¹ Xiaoyi Pan,¹ and Guoyu Wang²

¹State Key Laboratory of Complex Electromagnetic Environment Effects on Electronics and Information System (CEMEE), National University of Defense Technology, Changsha 410073, China

²School of Electronic Science and Engineering, National University of Defense Technology, Changsha 410073, China

Correspondence should be addressed to Xiaoyi Pan; pan_xiao_yi@hotmail.com

Received 15 April 2017; Revised 8 June 2017; Accepted 2 July 2017; Published 14 August 2017

Academic Editor: Ana Alejos

Copyright © 2017 Dejun Feng et al. This is an open access article distributed under the Creative Commons Attribution License, which permits unrestricted use, distribution, and reproduction in any medium, provided the original work is properly cited.

V-FM waveforms, composed of two chirp signals with the opposite slopes, can also achieve high range resolution with wide bandwidth via intrapulse frequency modulation. In this paper, a framework for inverse synthetic aperture radar (ISAR) imaging of moving targets with V-FM waveforms is investigated, where the range compression of the received signals is achieved by the dual-channel dechirping and the azimuth compression is done via the traditional Fourier transform (FT). The two corresponding reconstructed temporary high-resolution range profiles (HRRPs) from the double channels are synthesized for the HRRPs of the target, in which one is flipped from left to right and added to the other. Then the final HRRPs are arranged into a two-dimensional (2D) array and the azimuth compression is done via FT to achieve the ISAR imaging after the motion compensation. Simulated trials, adopting the scattering center modeling of the Yak-42 plane, are used to validate the correctness of the analyses and the finally well-focused images greatly support the effectiveness of V-FM waveforms in ISAR imaging.

1. Introduction

Inverse synthetic aperture radar (ISAR) is a powerful tool in many civilian and military fields such as air traffic control, harbor and river traffic surveillance, and remote sensing of satellites, benefiting from the superiorities such as robust performance under all-weather conditions, high-resolution images, and long detection range [1–8]. The high-resolution image even can be utilized for the purposes of feature extraction and target recognition of noncooperative targets [9–11]. In order to improve the range resolution and the detection range, large time-bandwidth product waveforms, such as chirp signal, frequency-stepped signal, and frequency-stepped chirp signal, are commonly utilized in modern imaging radar systems [9, 12–16]. The superiority of chirp signal is that it can improve the range resolution while maintaining a high signal-to-noise ratio (SNR) via intrapulse frequency modulation and pulse compression technology. However, due to the “ridge” ambiguity function of chirp signals, inevitable ambiguity appears in range and velocity. Frequency-stepped

signal, achieving high range resolution without expensive hardware to support the instantaneous wide bandwidth, takes relatively long time duration to complete the transmitting and receiving process of each burst.

V-FM signal, possessing a “thumbtack” ambiguity function as mentioned in [17], is potential in mitigating the ambiguity appearing in range and velocity while achieving high-resolution range profiles (HRRPs). Since V-FM waveforms are composed of two chirp signals with the opposite slopes, range compression can be achieved by the dual-channel matched filtering (MF). According to the Shannon-Nyquist sampling theorem, a signal can be reconstructed exactly from measurements uniformly sampled by an analogue-to-digital converter (ADC) whose sampling rate must be at least twice the maximum frequency of the signal. Thus, a high quality ADC is extremely needed to recover the wideband V-FM signal which may become practically infeasible. Fortunately, dechirping algorithm can also achieve pulse compression of chirp waveforms while reducing the sampling rate of ADC significantly. The concept of dechirping is to distinguish

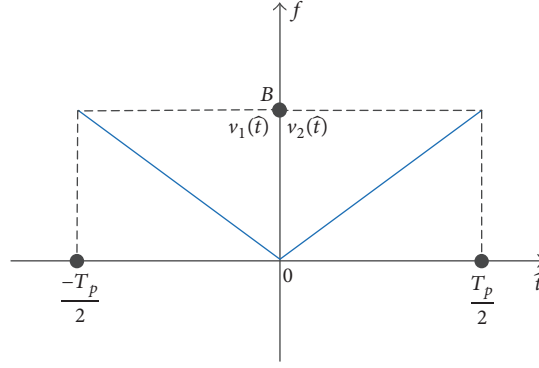


FIGURE 1: Sketch map of V-FM waveforms in time-frequency plane.

scattering centers in different downrange bins with lower sampling rate compared with MF-based methods, in which the wideband waveforms are mixed with a reference signal with the same chirp rate as the transmitted chirp signal. After dechirping processing, signals of the scattering centers in different downrange bins are referred to corresponding single frequencies. Then after the Fourier transform (FT), single frequencies can be resolved and the HRRPs are also achieved. In the applications of wideband inverse synthetic aperture radar (ISAR) imaging, the reconstructed HRRPs are rearranged into a two-dimensional (2D) matrix (the number of range cells against the number of pulses) and the final ISAR image can be obtained via the azimuth compression algorithm on the 2D matrix after target motion compensation [18].

Due to the special characteristics of the V-FM waveforms, a dual-channel dechirping algorithm is proposed to recover the HRRPs of moving targets in this paper. The main idea of dual-channel dechirping of wideband V-FM waveforms is that two independent HRRPs are reconstructed from the two independent channels with dechirping processing and one is flipped from left to right and added to the other to synthesize the final HRRPs. Then the rearranged 2D matrix of synthesized HRRPs is utilized to form the ISAR image after motion compensation.

This paper is organized as follows. The pulse compression via dual-channel dechirping is discussed in detail in Section 2. In Section 3, HRRPs synthesis of wideband V-FM waveforms after the dual-channel dechirping and ISAR image formation are addressed. Simulated results are carried out in Section 4 to validate the effectiveness of the proposed algorithm and the conclusions are made in Section 5.

2. Signal Model of V-FM Waveforms

The signal model of wideband V-FM waveforms and the corresponding pulse compression of moving targets via dual-channel dechirping are devoted in this section.

2.1. Signal Modeling. Assume that the complex V-FM waveform in zero intermediate frequency form is composed of two

chirp signals with the opposite slopes as shown in Figure 1, which follows

$$v(t) = \text{rect}\left(\frac{\hat{t}}{T_p}\right) \cdot (v_1(\hat{t}) + v_2(\hat{t})), \quad (1)$$

where \hat{t} represents the fast time, T_p is the pulse width, \cdot is the multiplicative operator, and $\text{rect}(\hat{t}/T_p)$ is the rectangle function which follows

$$\text{rect}\left(\frac{\hat{t}}{T_p}\right) = \begin{cases} 1, & \hat{t} \in \left[-\frac{T_p}{2}, \frac{T_p}{2}\right], \\ 0, & \text{else,} \end{cases}$$

$$v_1(\hat{t}) = \begin{cases} \exp(-j\pi\gamma\hat{t}^2), & \hat{t} \in [-\infty, 0], \\ 0, & \hat{t} \in [0, \infty], \end{cases} \quad (2)$$

$$v_2(\hat{t}) = \begin{cases} 0, & \hat{t} \in [-\infty, 0], \\ \exp(-j\pi\gamma\hat{t}^2), & \hat{t} \in [0, \infty]. \end{cases}$$

γ is the chirp rate and the bandwidth $B = \gamma T_p$. Redefine two-rectangle function:

$$\text{rect}_{\text{half}}^+\left(\frac{\hat{t}}{T_p}\right) = \begin{cases} 1, & \hat{t} \in \left[0, \frac{T_p}{2}\right], \\ 0, & \text{else,} \end{cases} \quad (3)$$

$$\text{rect}_{\text{half}}^-\left(\frac{\hat{t}}{T_p}\right) = \begin{cases} 1, & \hat{t} \in \left[-\frac{T_p}{2}, 0\right], \\ 0, & \text{else} \end{cases}$$

and then (1) can be rewritten as

$$v(t) = \text{rect}_{\text{half}}^-\left(\frac{\hat{t}}{T_p}\right) \cdot v_1(\hat{t}) + \text{rect}_{\text{half}}^+\left(\frac{\hat{t}}{T_p}\right) \cdot v_2(\hat{t}). \quad (4)$$

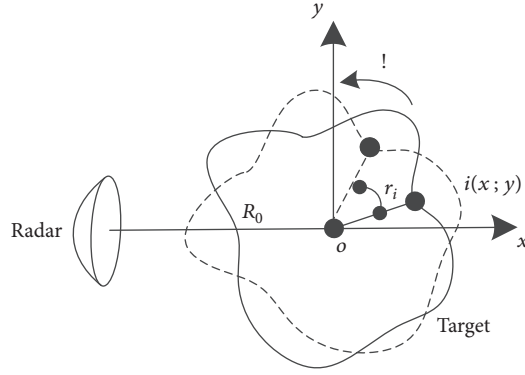


FIGURE 2: Geometry of ISAR imaging.

After the upconversion, we have the transmitted V-FM waveform as follows:

$$\begin{aligned}
 s(\hat{t}, t_m) &= v(\hat{t}) \cdot \exp(j2\pi f_0 t) \\
 &= \text{rect}_{\text{half}}^{-} \left(\frac{\hat{t}}{T_p} \right) \cdot \exp \left(j2\pi \left(f_0 t - \frac{1}{2} \gamma \hat{t}^2 \right) \right) \\
 &\quad + \text{rect}_{\text{half}}^{+} \left(\frac{\hat{t}}{T_p} \right) \\
 &\quad \cdot \exp \left(j2\pi \left(f_0 t + \frac{1}{2} \gamma \hat{t}^2 \right) \right),
 \end{aligned} \tag{5}$$

where f_0 is the carrier frequency, t_m is the slow time, t is the full time, and $\hat{t} = t - t_m$. Suppose that the pulse repetition interval (PRI) of radar is T_{PRI} ; then $t_m = mT_{\text{PRI}}$.

The geometry of ISAR imaging is shown in Figure 2. The local coordinate system xoy is embedded on the target with the radar line of sight (LOS) being the x -axis and the point o on the target is chosen as the origin. The target has the circular motion with a rotation rate ω rad/s and the range from ISAR to o is denoted as R_0 . Consider a scattering center $i(x, y)$ on a moving target with σ_i being the scattering coefficient and $R_i \approx R_0 + x + y\omega t_m$ being the range from scattering center i to ISAR; the echo of the scattering center i can be written as

$$\begin{aligned}
 s_r(\hat{t}, t_m) &= \sigma_i s \left(\hat{t} - \frac{2R_i}{c}, t_m \right) \\
 &= \text{rect}_{\text{half}}^{-} \left(\frac{\hat{t} - 2R_i/c}{T_p} \right) \\
 &\quad \cdot \exp \left(j2\pi \left(f_0 \left(t - \frac{2R_i}{c} \right) - \frac{1}{2} \gamma \left(\hat{t} - \frac{2R_i}{c} \right)^2 \right) \right) \\
 &\quad + \text{rect}_{\text{half}}^{+} \left(\frac{\hat{t} - 2R_i/c}{T_p} \right) \\
 &\quad \cdot \exp \left(j2\pi \left(f_0 \left(t - \frac{2R_i}{c} \right) + \frac{1}{2} \gamma \left(\hat{t} - \frac{2R_i}{c} \right)^2 \right) \right),
 \end{aligned} \tag{6}$$

where c is the speed of the electromagnetic wave. For the sake of notation simplicity, the dependence of R_i on t_m will be omitted in the subsequently equations.

2.2. Pulse Compression via Dual-Channel Dechirping. The reference signals of the two channels can be expressed, respectively, as

$$\begin{aligned}
 s_{\text{ref-1}}(\hat{t}, t_m) &= \text{rect}_{\text{half}}^{-} \left(\frac{\hat{t} - 2R_{\text{ref}}/c}{T_{\text{ref}}} \right) \\
 &\quad \cdot \exp \left(j2\pi \left(f_0 (t - T_{\text{ref}}) - \frac{1}{2} \gamma (\hat{t} - T_{\text{ref}})^2 \right) \right),
 \end{aligned} \tag{7}$$

$$\begin{aligned}
 s_{\text{ref-2}}(\hat{t}, t_m) &= \text{rect}_{\text{half}}^{+} \left(\frac{\hat{t} - 2R_{\text{ref}}/c}{T_{\text{ref}}} \right) \\
 &\quad \cdot \exp \left(j2\pi \left(f_0 (t - T_{\text{ref}}) + \frac{1}{2} \gamma (\hat{t} - T_{\text{ref}})^2 \right) \right),
 \end{aligned} \tag{8}$$

where R_{ref} is the reference range, T_{ref} is the reference pulse duration, and $T_{\text{ref}} = 2R_{\text{ref}}/c$.

The time-domain compressed signals of the two channels after dechirping are given as follows:

$$\begin{aligned}
 s_{\text{if-1}}(\hat{t}, t_m) &= \text{rect}_{\text{half}}^{-} \left(\frac{\hat{t} - 2R_i/c}{T_p} \right) \\
 &\quad \cdot \exp \left(\frac{j4\pi\gamma}{c} \left(\hat{t} - \frac{2R_{\text{ref}}}{c} \right) R_{\Delta} \right) \\
 &\quad \cdot \exp \left(\frac{-j4\pi\gamma}{c^2} R_{\Delta}^2 \right) \\
 &\quad \cdot \exp \left(\frac{-j4\pi f_0 R_{\Delta}}{c} \right),
 \end{aligned} \tag{9}$$

$$\begin{aligned}
 s_{\text{if-2}}(\hat{t}, t_m) &= \text{rect}_{\text{half}}^{+} \left(\frac{\hat{t} - 2R_i/c}{T_p} \right) \\
 &\quad \cdot \exp \left(\frac{-j4\pi\gamma}{c} \left(\hat{t} - \frac{2R_{\text{ref}}}{c} \right) R_{\Delta} \right) \\
 &\quad \cdot \exp \left(\frac{j4\pi\gamma}{c^2} R_{\Delta}^2 \right) \cdot \exp \left(\frac{-j4\pi f_0 R_{\Delta}}{c} \right),
 \end{aligned}$$

where $R_{\Delta} = R_i - R_{\text{ref}}$.

The first exponentials of $s_{\text{if-1}}(\hat{t}, t_m)$ and $s_{\text{if-2}}(\hat{t}, t_m)$ in (9) are the range items which produce beat frequencies $2\gamma R_\Delta/c$ and $-2\gamma R_\Delta/c$, respectively. The second exponentials of $s_{\text{if-1}}(\hat{t}, t_m)$ and $s_{\text{if-2}}(\hat{t}, t_m)$ in (9) account for Doppler and the third exponentials are the residual video phase (RVP). The RVP of each channel can be removed by the translation motion compensation (TMC) algorithms [7]. Taking FT of in (9) in terms of t , the two temporary HRRPs of the double channels in the frequency domain, after the two RVPs and constant terms are removed, are obtained as follows:

$$\begin{aligned} S_{\text{if-1}}(f, t_m) &= \frac{T_p \sigma_i}{2} \sin c \left(\frac{T_p}{2} \left(f - \frac{2\gamma R_\Delta}{c} \right) \right) \\ &\quad \cdot \exp \left(\frac{-j4\pi f_0 R_\Delta}{c} \right), \\ S_{\text{if-2}}(f, t_m) &= \frac{T_p \sigma_i}{2} \sin c \left(\frac{T_p}{2} \left(f + \frac{2\gamma R_\Delta}{c} \right) \right) \\ &\quad \cdot \exp \left(\frac{-j4\pi f_0 R_\Delta}{c} \right). \end{aligned} \quad (10)$$

It can be seen that the two temporary HRRPs form the dual-channel dechirping being with the same amplitude but symmetrical about zero in the frequency domain.

3. HRRPs Synthesis and ISAR Image Formation

After the two temporary HRRPs are achieved, the second temporary HRRPs $S_{\text{if-2}}(f, t_m)$ can be flipped from left to right and we have

$$\begin{aligned} S'_{\text{if-2}}(f, t_m) &= \text{fliplr}_f(S_{\text{if-2}}(f, t_m)) \\ &= \frac{T_p \sigma_i}{2} \sin c \left(\frac{T_p}{2} \left(f - \frac{2\gamma R_\Delta}{c} \right) \right) \\ &\quad \cdot \exp \left(\frac{-j4\pi f_0 R_\Delta}{c} \right), \end{aligned} \quad (11)$$

where $\text{fliplr}_f(\cdot)$ represents flipping the left part of the HRRPs to the right part of them in frequency domain. Then the finally synthesized HRRPs can be obtained as

$$\begin{aligned} S_{\text{if}}(f, t_m) &= S_{\text{if-1}}(f, t_m) + S'_{\text{if-2}}(f, t_m) \\ &= T_p \sigma_i \sin c \left(\frac{T_p}{2} \left(f - \frac{2\gamma R_\Delta}{c} \right) \right) \\ &\quad \cdot \exp \left(\frac{-j4\pi f_0 R_\Delta}{c} \right). \end{aligned} \quad (12)$$

After multiplying a constant conversion coefficient $2\gamma/c$, the HRRPs in the original frequency domain can be transformed into the downrange domain as

$$\begin{aligned} S_{\text{if}}(r, t_m) &= T_p \sigma_i \sin c \left(\frac{\gamma T_p}{c} (r - R_\Delta) \right) \\ &\quad \cdot \exp \left(\frac{-j4\pi f_0 R_\Delta}{c} \right), \end{aligned} \quad (13)$$

where r represents the downrange domain.

TABLE 1: The simulation parameters.

Carrier frequency	f_0	10 GHz
Bandwidth	B	300 MHz
Pulse width	T_p	100 μ s
PRI	T_{PRI}	1 KHz

Without loss of generality, let the reference range $R_{\text{ref}} = R_0$ and after motion compensation [19, 20], we have

$$R_\Delta = x + y\omega t_m. \quad (14)$$

Thus, the Doppler frequency of scattering center $i(x, y)$ can be calculated as

$$f_d = \frac{1}{2\pi} \cdot \frac{4\pi f_0}{c} \cdot \frac{dR_\Delta}{dt_m} = \frac{2f_0 \omega y}{c}. \quad (15)$$

Then after the azimuth compression via FT, the final ISAR image formation follows as

$$\begin{aligned} I(r, f_m) &= T_p T_M \sigma_i \sin c \left(\frac{\gamma T_p}{c} (r - R_\Delta) \right) \\ &\quad \cdot \sin c (T_M (f_m - f_d)), \end{aligned} \quad (16)$$

where T_M denotes the whole observation time and f_m is the Doppler domain. Then the cross-range scaling of ISAR image can be achieved by $\rho_a = c/2f_0 T_M \omega$, after the rotation rate ω rad/s of moving targets is known or estimated [21, 22].

The flow chart of HRRPs reconstruction after the RVP of each channel is removed and ISAR image formation with wideband V-FM waveforms via dual-channel dechirping are shown in Figure 3.

4. Simulated Results

To analyze the performance of the proposed HRRPs reconstruction and ISAR image formation via the dual-channel dechirping technique, two aspects should be counted: the reconstructed HRRPs and the ultimate ISAR image after azimuth compression. We simulate radar echoes of moving targets with simple and complex shapes (Yak-42 model) to validate the effect of wideband V-FM waveforms in the applications of high-resolution ISAR imaging. The carrier frequency and the signal bandwidth of the V-FM waveforms are $f_0 = 10$ GHz in X-band and $B = 300$ MHz, respectively. The radar pulse width is 100 μ s and the PRI is 1 KHz. Then the range resolution is $\rho_r = c/2B = 0.5$ m and the main parameters of Sections 4.1, 4.2, and 4.3 are listed in Table 1. The number of downrange samples of each channel is 128; thus the total number of downrange samples is 256 which is much less than that in conventional pulse compression algorithms under the Shannon-Nyquist sampling theorem, such as MF.

4.1. Reconstructed HRRPs of Simple Target. The modeling of the simplest target is shown in Figure 4(a); there are seven dominant scattering centers with coordinates $(-8, 0)$, $(-5, 0)$,

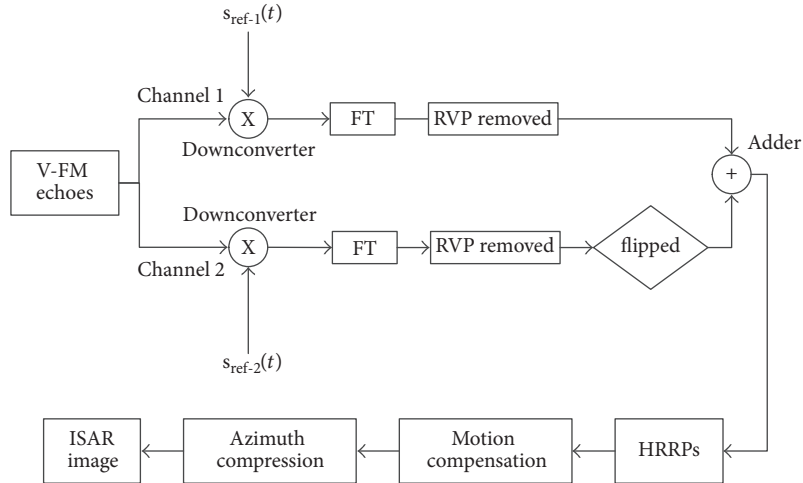


FIGURE 3: Flow chart of ISAR imaging with wideband V-FM waveforms.

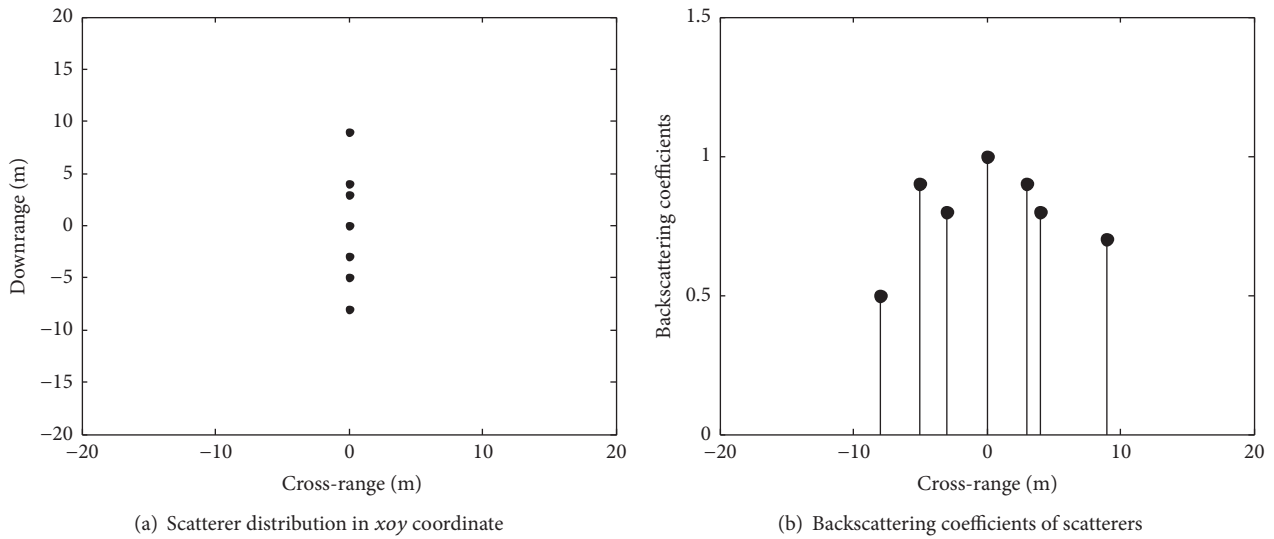


FIGURE 4: Modeling of the simple target.

(-3, 0), (0, 0), (3, 0), (4, 0), and (9, 0) (units in meters) in different downrange bins. The corresponding backscattering coefficients are 0.5, 0.9, 0.8, 1, 0.9, 0.8, and 0.7, respectively. The real position in downrange and amplitude of the seven dominant scattering centers are depicted in Figure 4(b).

In high SNR scenarios (SNR = 20 dB), the two recovered HRRPs of the dual-channel dechirping are shown in Figures 5(a) and 5(b). The position and amplitude of each scatterer (namely, the real HRRPs) are represented by the red dotted lines in Figure 5. It can be seen that the recovered HRRPs of channel 2 are symmetrical about zero with that of channel 1. After the left part of recovered HRRPs of channel 2 is flipped to the right, the HRRPs shown in Figure 5(c) are with the same position and amplitude as the HRRPs of channel 1 shown in Figure 5(a).

The finally synthesized HRRPs shown in Figure 5(d) via the addition of temporary HRRPs of channel 1 and channel 2 are robust which is also in accordance with the real HRRPs accurately. It should be noted that since the V-FM waveforms are coherent while the noises are independent, the SNR of synthesized HRRPs are twice that of single HRRPs from channel 1 and channel 2 actually.

4.2. Reconstructed HRRPs of Simple Target with Various SNRs.

Gaussian distributed complex noise with four groups of SNRs, 5 dB, 0 dB, -5 dB, and -10 dB, are adopted here to illuminate the effect of the HRRPs reconstruction algorithm in a more realistic scenario.

The synthesized HRRPs are shown in Figure 6 and it can be seen that artificial scattering centers in the reconstructed

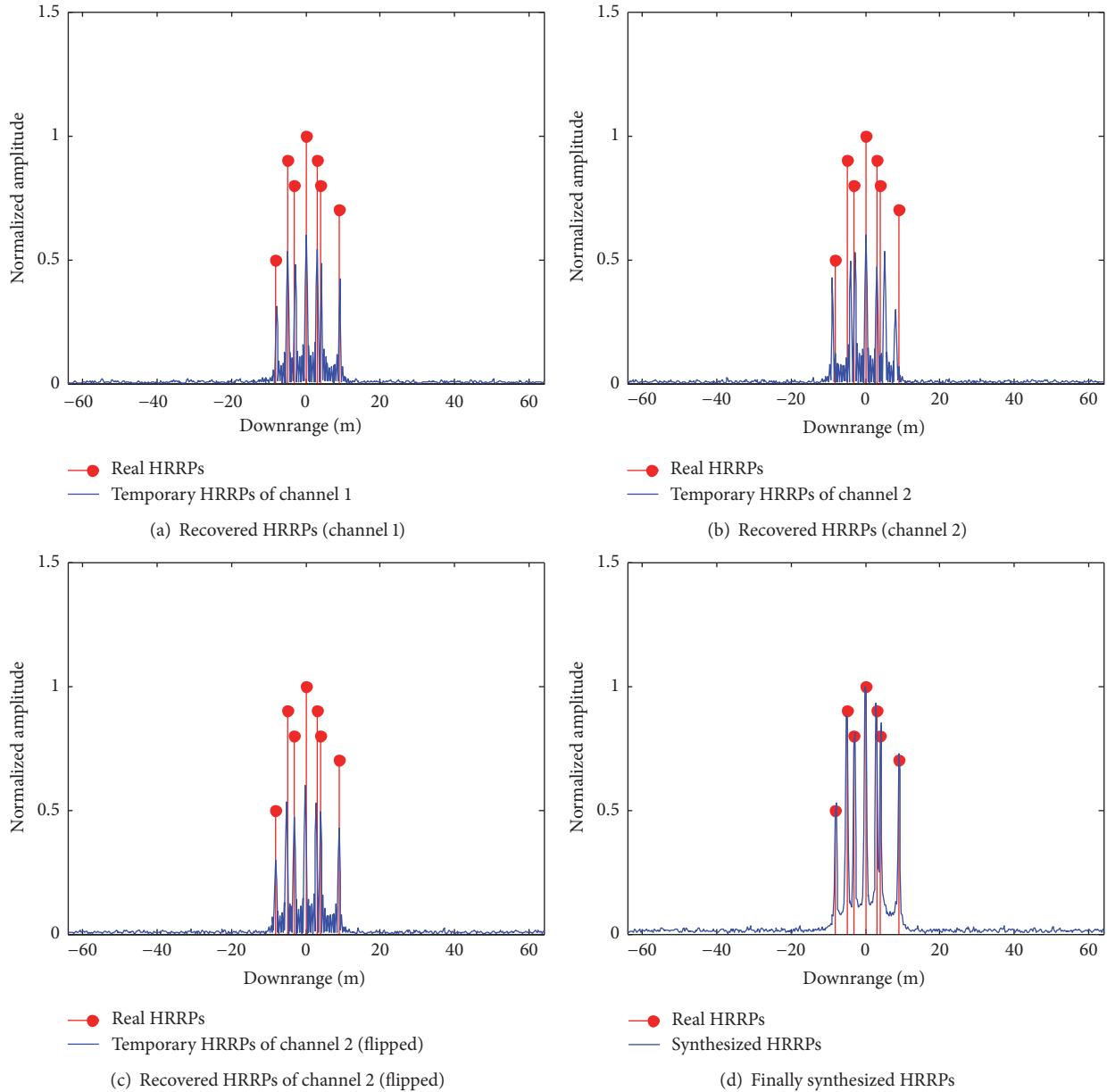


FIGURE 5: HRRPs reconstruction (SNR = 20 dB).

HRRPs increase with the SNR decreases. Further, it can be observed that the recovered HRRPs are robust when SNR = 5 dB and 0 dB shown in Figures 6(a) and 6(b). However, when SNR is less than -5 dB, the weak scatterers in the recovered HRRPs cannot be distinguished from the noise as shown in Figure 6(c) and the reconstructed HRRPs are contaminated by the noise significantly when SNR = -10 dB, as shown in Figure 6(d).

4.3. ISAR Image Formation of Yak-42 Model. To demonstrate the effect of wideband V-FM waveforms in ISAR imaging, 256 pulses with a time duration $T_M = 0.256$ s are transmitted and collected to yield the 2D ISAR image formation. A Yak-42 plane model of 330 scatterers is adopted in the following simulations as shown in Figure 7, which takes up to 35 m

(downrange) \times 30 m (cross-range). Suppose that the rotation rate $\omega = 0.05 \times 2\pi$ (rad/s); thus the resolution of azimuth can be calculated as $\rho_a = c/2f_0 T_M \omega = 0.1865$ m.

The 256 pulses are referred to the reconstructed 256 HRRPs which can be rearranged into a 2D matrix to achieve the ISAR image after standard motion compensation. Comparing the 256 HRRPs of channel 1 shown in Figure 8(a) with those of channel 2 shown in Figure 8(b), it can be concluded that HRRPs of the two channels are symmetrical about the zero. The synthesized HRRPs of the two channels are presented in Figure 8(c) in which the amplitude is almost twice that in Figures 8(a) and 8(b). The ultimately focused ISAR image (after the cross-range scaling) is shown in Figure 8(d), under a high SNR = 20 dB.

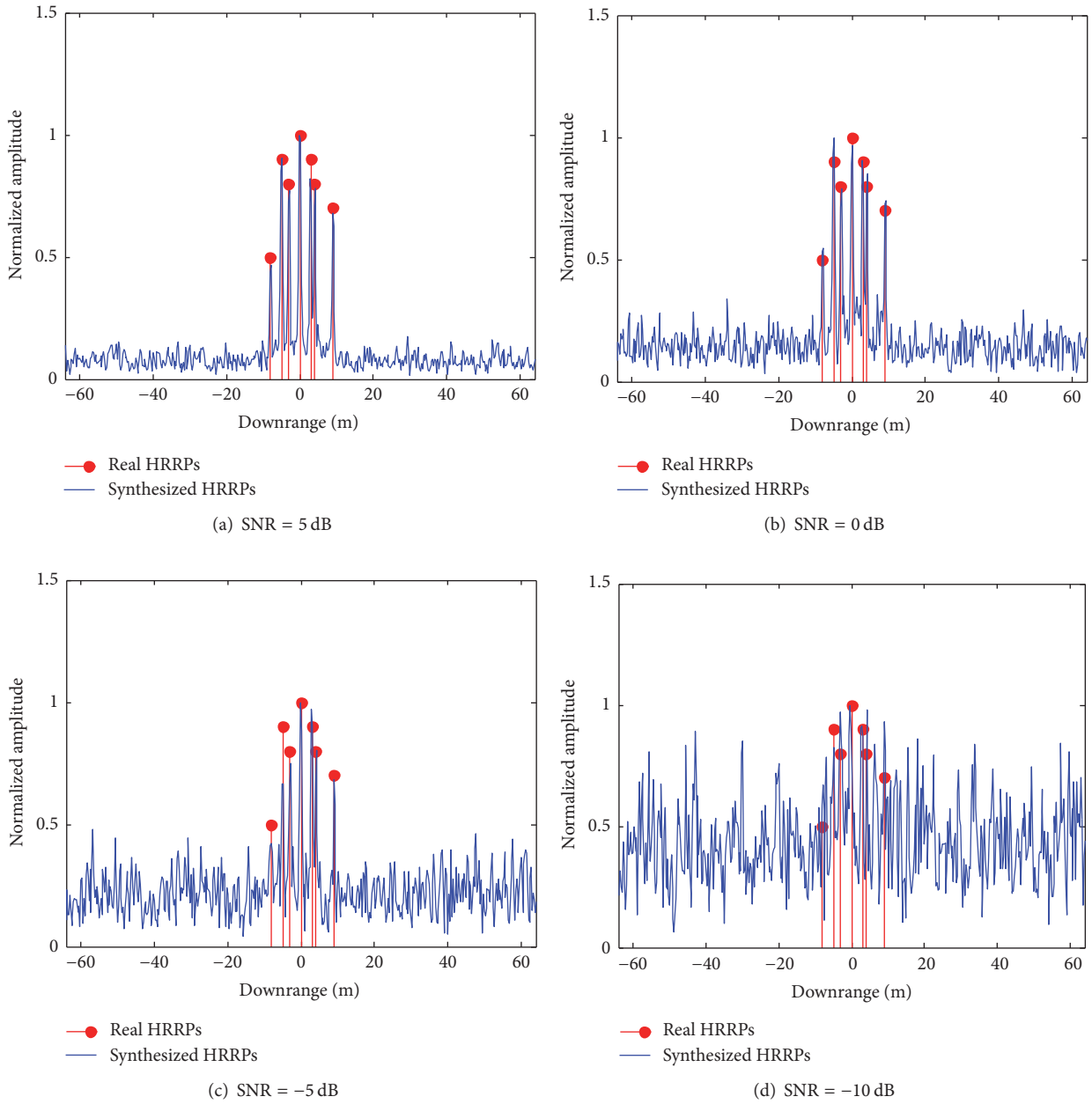


FIGURE 6: HRRPs reconstruction with various SNRs.

Similar to Section 4.2, four groups of Gaussian distributed complex noise with SNRs, 5 dB, 0 dB, -5 dB and -10 dB, are added to the 256 collected echoes and the corresponding ISAR imaging results are shown in Figure 9.

In a high SNR case, for example, SNR = 5 dB and SNR = 0 dB shown in Figures 9(a) and 9(b), the ISAR images are focused and the scatterers are clearly distinguished. However, when SNR = -5 dB, some weak scatterers of the plane are covered by the noise and the ISAR image of the plane is almost invisible when the SNR = -10 dB. From the four simulated results with noise, the analyses in Section 4.2 are demonstrated.

5. Conclusions

Based on the characteristics of wideband V-FM waveforms, both of the MF and the dechirping algorithms can be applied on the HRRPs reconstruction. The novelty of this paper is that it proposed and validated the effect of wideband V-FM waveforms in the application of HRRPs reconstruction and ISAR imaging of moving targets. Via dual-channel dechirping, the finally synthesized HRRPs from the two independent channels were robust and in accordance with the real HRRPs and the final ISAR image formation was also focused under high SNR conditions. Under

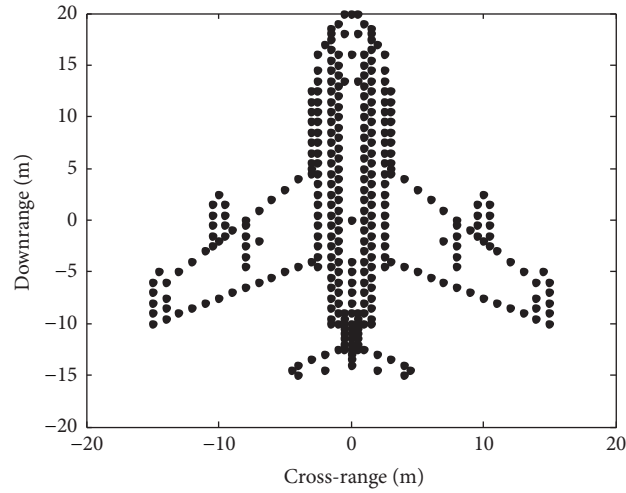


FIGURE 7: Model of Yak-42 plane with 330 scatterers.

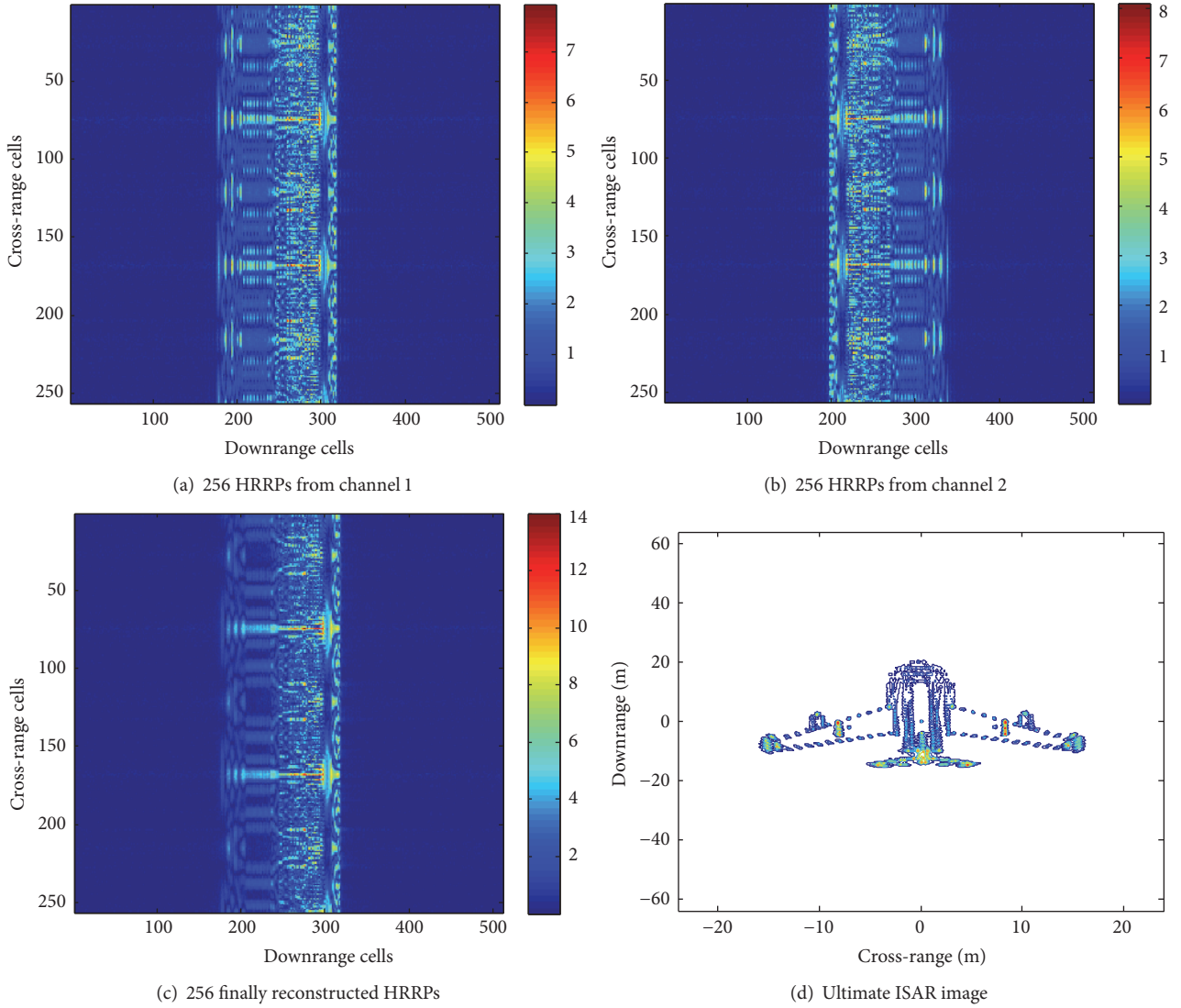


FIGURE 8: ISAR image formation of the Yak-42 plane model (SNR = 20 dB).

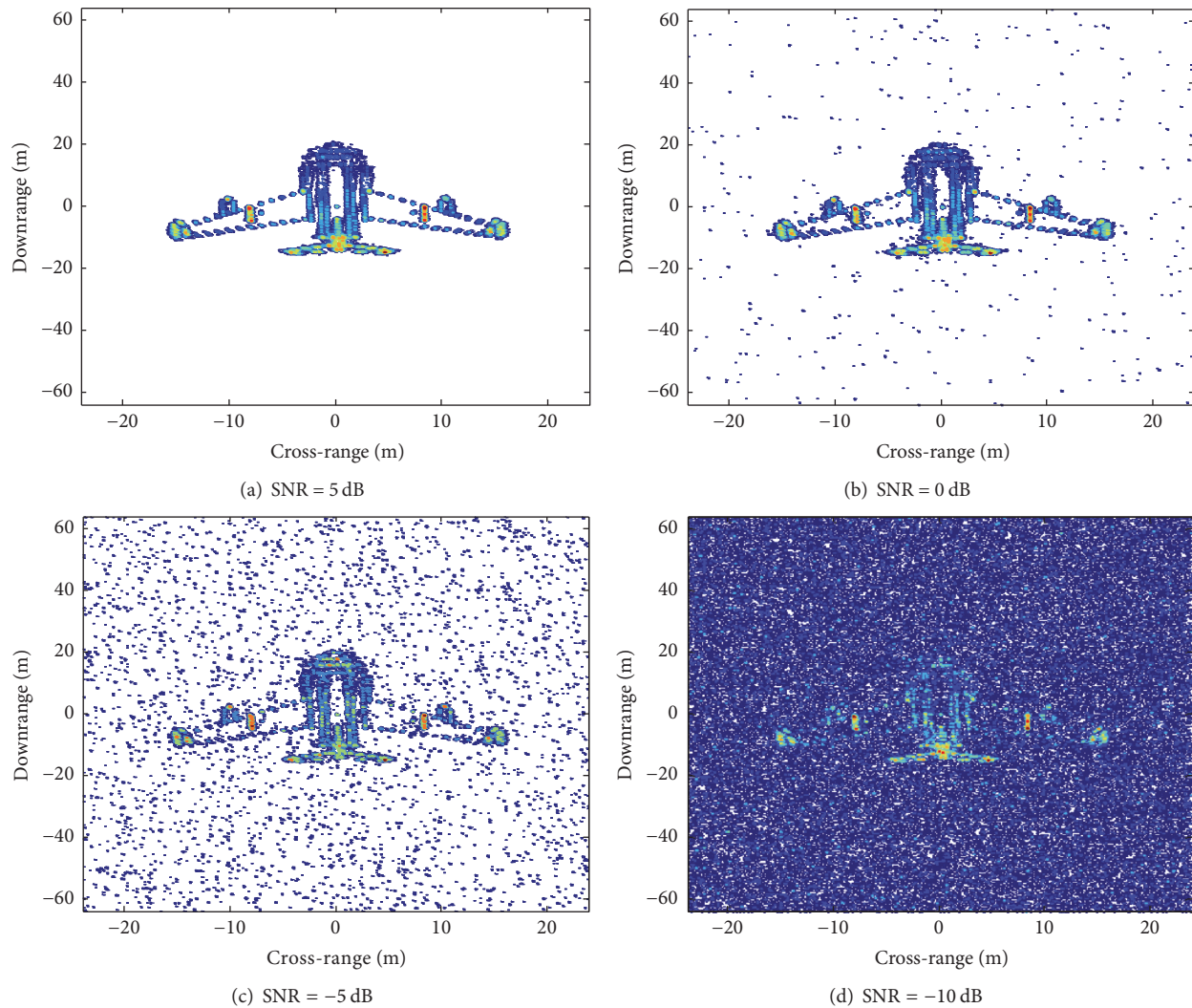


FIGURE 9: ISAR image formation of the Yak-42 plane model with various SNRs.

various SNRs, the recovered HRRPs of wideband V-FM waveforms were also addressed which reveals that the reconstructed HRRPs were robust when SNR is no less than -10 dB.

Conflicts of Interest

The authors declare that there are no conflicts of interest regarding the publication of this paper.

Acknowledgments

The authors would like to thank Dr. Lei Zhang for providing the modeling data of Yak-42. This work was supported by the National Natural Science Foundation of China under Grant 61571451.

References

- [1] Z.-S. Liu, R. Wu, and J. Li, "Complex ISAR imaging of maneuvering targets via the Capon estimator," *IEEE Transactions on Signal Processing*, vol. 47, no. 5, pp. 1262–1271, 1999.
- [2] G. Wang, X.-G. Xia, and V. C. Chen, "Three-Dimensional ISAR imaging of maneuvering targets using three receivers," *IEEE Transactions on Image Processing*, vol. 10, no. 3, pp. 436–447, 2001.
- [3] X. Bai, F. Zhou, M. Xing, and Z. Bao, "Scaling the 3-D image of spinning space debris via bistatic inverse synthetic aperture radar," *IEEE Geoscience and Remote Sensing Letters*, vol. 7, no. 3, pp. 430–434, 2010.
- [4] L. Zhang, M. Xing, C.-W. Qiu et al., "Resolution enhancement for inversed synthetic aperture radar imaging under low SNR via improved compressive sensing," *IEEE Transactions on Geoscience and Remote Sensing*, vol. 48, no. 10, pp. 3824–3838, 2010.
- [5] G. Xu, M. Xing, L. Zhang, Y. Liu, and Y. Li, "Bayesian inverse synthetic aperture radar imaging," *IEEE Geoscience and Remote Sensing Letters*, vol. 8, no. 6, pp. 1150–1154, 2011.
- [6] Y. J. Huang, X. Wang, X. Li, and B. Moran, "Inverse synthetic aperture radar imaging using frame theory," *IEEE Transactions on Signal Processing*, vol. 60, no. 10, pp. 5191–5200, 2012.
- [7] V. C. Chen and M. Martorella, "Inverse synthetic aperture radar imaging: Principles, algorithms and applications," *Inverse*

Synthetic Aperture Radar Imaging: Principles, Algorithms and Applications, pp. 1–290, 2014.

- [8] F. Berizzi, M. Martorella, and E. Giusti, *Radar Imaging for Maritime Observation, Signal and Image Processing of Earth Observations*, Taylor & Francis Inc, 2016.
- [9] Y. Luo, Q. Zhang, C.-W. Qiu, X.-J. Liang, and K.-M. Li, “Micro-Doppler effect analysis and feature extraction in ISAR imaging with stepped-frequency chirp signals,” *IEEE Transactions on Geoscience and Remote Sensing*, vol. 48, no. 4, pp. 2087–2098, 2010.
- [10] K.-M. Li, X.-J. Liang, Q. Zhang, Y. Luo, and H.-J. Li, “Micro-doppler signature extraction and ISAR imaging for target with micromotion dynamics,” *IEEE Geoscience and Remote Sensing Letters*, vol. 8, no. 3, pp. 411–415, 2011.
- [11] P. Lei, J. Sun, J. Wang, and W. Hong, “Micromotion parameter estimation of free rigid targets based on radar micro-doppler,” *IEEE Transactions on Geoscience and Remote Sensing*, vol. 50, no. 10, pp. 3776–3786, 2012.
- [12] K. L. Sitler, M. A. Temple, R. C. Novack, and J. A. Hughes, “High range resolution profiling using phase-coded, stepped-frequency waveforms,” *Electronics Letters*, vol. 38, no. 1, pp. 46–48, 2002.
- [13] Q. Zhang, T. S. Yeo, and G. Du, “ISAR imaging in strong ground clutter using a new stepped-frequency signal format,” *IEEE Transactions on Geoscience and Remote Sensing*, vol. 41, no. 5, pp. 948–952, 2003.
- [14] F. Zhu, Q. Zhang, Q. Lei, and Y. Luo, “Reconstruction of moving target’s HRRP using sparse frequency-stepped chirp signal,” *IEEE Sensors Journal*, vol. 11, no. 10, pp. 2327–2334, 2011.
- [15] L. Zhang, Z.-J. Qiao, M. D. Xing, Y. C. Li, and Z. Bao, “High-resolution ISAR imaging with sparse stepped-frequency waveforms,” *IEEE Transactions on Geoscience and Remote Sensing*, vol. 49, no. 11, pp. 4630–4651, 2011.
- [16] J. Yang, X. Huang, T. Jin, J. Thompson, and Z. Zhou, “Synthetic aperture radar imaging using stepped frequency waveform,” *IEEE Transactions on Geoscience and Remote Sensing*, vol. 50, no. 5, pp. 2026–2036, 2012.
- [17] A. Freedman and N. Levanon, “Staggered Costas Signals,” *IEEE Transactions on Aerospace and Electronic Systems*, vol. 22, no. 6, pp. 695–702, 1986.
- [18] E. Giusti and M. Martorella, “Range doppler and image autofocusing for FMCW inverse synthetic aperture radar,” *IEEE Transactions on Aerospace and Electronic Systems*, vol. 47, no. 4, pp. 2807–2823, 2011.
- [19] H. Wu, D. Grenier, G. Y. Delisle, and D.-G. Fang, “Translational Motion Compensation in ISAR Image Processing,” *IEEE Transactions on Image Processing*, vol. 4, no. 11, pp. 1561–1571, 1995.
- [20] S. Zhang, Y. Liu, and X. Li, “Fast entropy minimization based autofocusing technique for ISAR imaging,” *IEEE Transactions on Signal Processing*, vol. 63, no. 13, pp. 3425–3434, 2015.
- [21] B.-S. Kang, J.-H. Bae, M.-S. Kang, E. Yang, and K.-T. Kim, “ISAR cross-range scaling via joint estimation of rotation center and velocity [Correspondence],” *IEEE Transactions on Aerospace and Electronic Systems*, vol. 52, no. 3, pp. 1454–1460, 2016.
- [22] M.-S. Kang, J.-H. Bae, B.-S. Kang, and K.-T. Kim, “ISAR cross-range scaling using iterative processing via principal component analysis and bisection algorithm,” *IEEE Transactions on Signal Processing*, vol. 64, no. 15, pp. 3909–3918, 2016.



Hindawi

Submit your manuscripts at
<https://www.hindawi.com>

